OPTICA QUANTUM

Bi-chromatic intensity squeezing using four-wave mixing in ^{85}Rb vapor

ZIQI NIU,[1,*] **JIANMING WEN,**[2] **CHUANWEI ZHANG,**[3] **SHENGWANG DU,**[4,5,6] **AND IRINA NOVIKOVA**[1]

[1] *Department of Physics, William & Mary, Williamsburg, Virginia 23187, USA*
[2] *Department of Electrical and Computer Engineering, Binghamton University, Binghamton, New York 13902, USA*
[3] *Department of Physics, Washington University in St. Louis, St. Louis, Missouri 63105, USA*
[4] *Department of Physics, The University of Texas at Dallas, Richardson, Texas 75080, USA*
[5] *Elmore Family School of Electrical and Computer Engineering, Purdue University, West Lafayette, Indiana 47907, USA*
[6] *Purdue Quantum Science and Engineering Institute, Purdue University, West Lafayette, Indiana 47907, USA*
*zniu01@wm.edu

Received 15 October 2024; revised 16 December 2024; accepted 7 January 2025; published 31 January 2025

We experimentally investigate four-wave mixing (FWM) in a diamond interaction scheme using ^{85}Rb vapor, and identify the optimal conditions for joint amplification and relative intensity squeezing of two optical fields: one near the ^{85}Rb D$_1$ optical transition ($\lambda = 794.6$ nm) and the other in the telecom O-band ($\lambda = 1324$ nm). We achieved a reduction of relative intensity noise by up to 2.6 ± 0.4 dB compared with the shot noise level, signifying the non-classical quantum correlations. The observed level of intensity squeezing is primarily limited by the available pump laser power, which constrains the achievable FWM gain. Numerical simulations show good agreement with the experimental results.

© 2025 Optica Publishing Group under the terms of the Optica Open Access Publishing Agreement

https://doi.org/10.1364/OPTICAQ.545134

Thanks to the rapid progress in quantum information science (QIS) over the past two decades, the number of potential QIS applications has expanded dramatically, ranging from quantum computing and quantum information processing to quantum cryptography and quantum sensing. The variety of physical platforms for these applications is also steadily increasing. Most quantum information carriers are based on electromagnetic radiation at a specified frequencies, making direct interfacing between different platforms highly challenging or even impossible [1,2]. This has renewed interest in solving the problem of interconnects—both local and remote—between various platforms [3,4]. An efficient frequency converter, capable of shifting the frequency of a quantum state without inducing decoherence, offers an ideal solution. Several such systems have been proposed and realized [5,6], many of which rely on nonlinear optical materials and often require a waveguide or cavity to achieve sufficient nonlinearity [7,8].

Nonlinear processes in hot or cold atoms present a promising alternative due to the strong enhancement of nonlinear interactions near atomic resonances. A double-ladder (or diamond) scheme in Rb or Cs atoms is particularly appealing for frequency conversion [9–11]. Given that alkali metal atoms have become a versatile platform for QIS, the double-ladder system could facilitate the conversion of their natural optical quantum carriers to the telecom bandwidth, enabling low-loss integration into quantum networks. Along this direction, several experiments have successfully demonstrated single-photon conversion using both cold and hot Rb vapor [9–14].

In this work, we focus on generating quantum fields, rather than single photons, to facilitate the implementation of quantum protocols based on continuous variables (CV), or qumodes [15–19], instead of discrete variables (DV) qubits [20–22]. Specifically, we investigate the generation of two optical fields at different frequencies with correlated quantum fluctuations, resulting in two-color, two-mode intensity squeezing. This process is driven by four-wave mixing (FWM) in a double-ladder scheme in ^{85}Rb, as illustrated in Fig. 1(a). The detunings are referenced to $5P_{3/2}, F' = 4$, $5P_{1/2}, F' = 2$ and 3 centeroid, and $6S_{1/2}, F' = 3$, respectively. In this scheme, two strong pump lasers at 780 nm (D2 Pump) and 1367 nm (IR Pump) excite atomic coherence between the $5S$ ground state and the $6S$ excited state, amplifying the probe field at 795 nm and producing a new conjugate field at 1324 nm. The photon numbers in these two fields are quantum-mechanically correlated. Conceptually, this approach is similar to FWM-based two-mode squeezing and entanglement generation in a double-Λ system, where up to 9 dB of squeezing has been demonstrated [23–25]. However, FWM in the double-ladder scheme is less efficient [26,27] due to faster decoherence, weaker available laser power, and larger Doppler mismatch. One potential solution is to operate closer to atomic resonance, but this leads to increased residual resonant absorption of the probe field, which degrades nonclassical correlations [28]. Consequently, the main experimental challenge

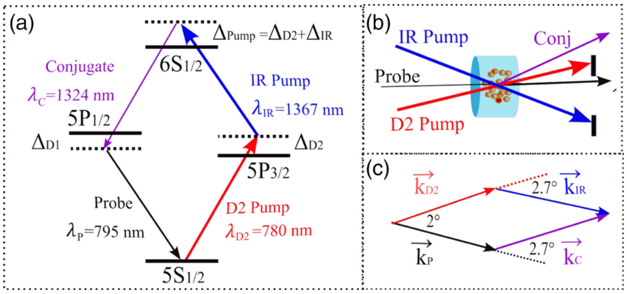

Fig. 1. (a) Double-ladder atomic configuration of ^{85}Rb employed in the experiment. (b) Experimental setup: the D2 pump (red) and IR pump (blue) are linearly polarized in the same direction and intersect inside the vapor cell with an orthogonally polarized probe beam (black). The conjugate field (purple) is generated with the same polarization as the probe. (c) Phase-matched four-wave mixing geometry of the optical fields within the vapor cell.

in this project was optimizing conditions where the FWM gain is sufficiently high and resonance losses are sufficiently low to observe two-mode squeezing. After optimization, we obtain a maximum intensity squeezing of −2.6 dB, corresponding to the FWM gain of approximately 2.1 (or ≈ 2.45 when accounting for losses). These results are in qualitative agreement with our numerical model and suggest that even better squeezing could be achieved with higher pump laser power.

The general experimental setup is depicted in Figs. 1(a)–1(c), with a detailed description of the apparatus provided in Ref. [29]. We use a 1.9 cm long pure ^{85}Rb cell with infrared anti-reflective (AR) coating, with the temperature maintained at 100.5°C. The cell is enclosed within three-layer μ-metal shielding to reduce the magnetic background Two intense pump optical fields couple the ground state $|1\rangle$ ($5S_{1/2}, F = 3$) to the excited state $|4\rangle$ ($6S_{1/2}$) through the intermediate state $|3\rangle$ ($5P_{3/2}$) via two cascaded optical transitions: $|1\rangle \rightarrow |3\rangle$ ($\lambda_{D2} = 780$ nm, $P_{D2} = 260$ mW, $d \approx 0.6$ mm) and $|3\rangle \rightarrow |4\rangle$ ($\lambda_{IR} = 1367$ nm, $P_{IR} = 35$ mW, $d \approx 0.4$ mm). These two nearly collinear laser beams intersect in a Rb vapor cell, producing FWM gain on the other two-photon transition pathway $|1\rangle \rightarrow |2\rangle(5P_{1/2}) \rightarrow |4\rangle$. As a result, a weak seeded probe field, tuned to the $|1\rangle \rightarrow |2\rangle$ transition ($\lambda_P = 795$ nm, probe power ≈ 600 μW, $d \approx 0.3$ mm), is amplified, and a fourth conjugate optical field at $\lambda_C = 1324$ nm is generated. All optical fields are linearly polarized, with the two pump fields sharing the same polarization, which is orthogonal to the polarization of the probe and conjugate fields. Orthogonal linear polarizations allow better filtering of harmful residual pump fields before the detector. All beams are generally well-overlapped across the cell length, with an effective length of ≈ 1.8 cm used for later modeling. The exact frequencies and relative orientation of the laser beams are determined by the phase-matching conditions

$$\begin{aligned} \Delta\vec{k} &= \vec{k}_{D2} + \vec{k}_{IR} - \vec{k}_P - \vec{k}_C = 0, \\ \Delta\omega &= \omega_{D2} + \omega_{IR} - \omega_P - \omega_C = 0, \end{aligned} \tag{1}$$

where ω_i and $\vec{k}_i$ are the frequencies and wave vectors of the optical fields, as labeled in Fig. 1(c). Note that the wave vectors $|\vec{k}_i| = \omega_i n_i / c$ account for variations in the refractive indices n_i due to both resonant linear and nonlinear optical dispersion (c is the speed of light in vacuum). In the experiment, $\Delta\vec{k}$ was adjusted to be approximately zero to maximize the FWM gain for the chosen input laser frequencies. For other detuning values, $\Delta\vec{k}$ was not zero due to frequency-dependent dispersion (see Supplement 1 for further details).

After the vapor cell, the probe and conjugate beams are directed to two photodiodes with quantum efficiencies of 95% for 795 nm and 85% for 1324 nm, respectively. Due to the wavelength mismatch between the probe and conjugate fields, the photon energies differ. Therefore, it is essential to measure and compare the photocurrents, which are proportional to the photon number rate in each field, rather than comparing light powers. We define the FWM generation efficiency, or gain $G_{P/C}$, as the ratio of the average photon number in the probe or conjugate field (respectively) after the cell ($z = L$) to the input photon number of the probe field at $z = 0$:

$$G_{P/C} = \frac{\langle \hat{n}_{P/C} \rangle (z = L)}{\langle \hat{n}_P \rangle (z = 0)}. \tag{2}$$

According to this definition, in the absence of FWM and optical losses, $G_P = 1$ and $G_C = 0$. As the strength of the FWM nonlinearity increases, the values of G_P and G_C become larger and closer to each other. In the absence of optical losses, G_P will always exceed G_C. However, if G_C surpasses G_P, it strongly indicates non-zero resonant losses in the probe field.

To identify the optimal operating conditions, we scanned the frequencies of the two pump lasers and measured the gain values for the probe and conjugate fields, G_P and G_C. Preliminary studies [29] showed that at low pump powers, the gain occurs almost exclusively when the pump fields are resonant with the corresponding optical transitions. However, at higher powers, it become possible to shift the frequency of the FWM gain peak farther from the optical resonance by optimizing the mutual orientation of the optical fields. Figure 2 presents an example of the measured probe and conjugate gain as a function of probe laser frequency, with the pump laser frequencies locked at a point that maximizes FWM gain near the wing of the probe optical transition. The conjugate field is created at several probe field frequencies where FWM occurs. As discussed, we deliberately optimized the beam geometry to maximize the FWM amplitude at the positive slope of the Doppler profile and shift it as far as possible from the center of the absorption line to minimize resonant absorption. While the available pump laser power was insufficient to push the FWM peak entirely outside the Doppler profile, we operated at a point where the residual resonant absorption for the probe field without FWM ranged between 60% and 80%. The additional modification of the probe absorption profile for probe red detuning (Δ_{D1}<0) is due to Autler–Towns splitting induced by the strong D_2 pump laser.

To understand the underlying physics behind our observation, we compared the measured output gain values for both the probe and conjugate fields with the predictions of the numerical model. In this model (detailed in the Supplement 1), we calculate the probe and conjugate output gain by incorporating the hyperfine structure of the $5S$, $5P$, and $6S$ atomic levels, as well as the thermal velocity distribution of the Rb atoms and the evolution of the optical fields as they propagate through the vapor. To achieve a good match for all probe field detunings, it was crucial to account for variations in optical dispersion, and consequently, changes in the phase-matching conditions $\Delta\vec{k}$, as defined in Eq. (1). Based on the refractive index calculations from the model, we estimate that the variations of the probe refractive index are relatively small near the gain region, but become more significant outside

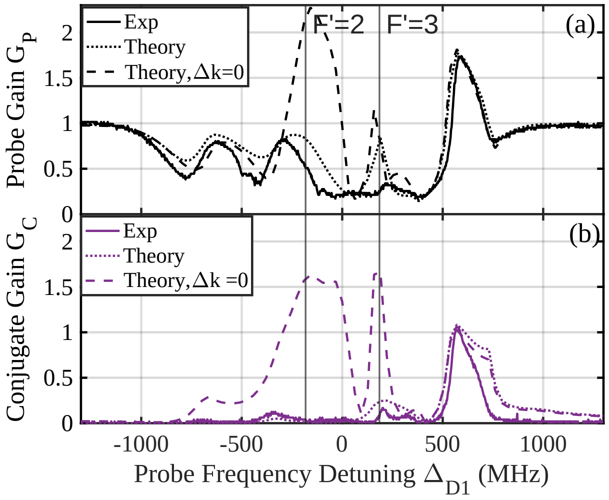

Fig. 2. Experimentally measured (solid lines) and simulated (dotted and dashed lines) probe and conjugate gains, (a) G_P and (b) G_C, are shown as functions of probe detuning Δ_{D1}. Zero detuning corresponds to the maximum resonance absorption, with vertical lines marking the positions of the $|5S_{1/2}, F = 3\rangle \rightarrow |5P_{1/2}, F = 2, 3\rangle$ optical resonances. For these measurements, the two pump detunings are set at $\Delta_{D2} = -280$ MHz and $\Delta_{IR} = 800$ MHz [30], with their respective powers: $P_{D2} = 260$ mW and $P_{IR} = 33$ mW. The maximum measured FWM gain values are $G_P = 1.73$ and $G_C = 1.05$ at a probe detuning of $\Delta_{D1} \approx 600$ MHz. The calculated spectra account for photodetector quantum efficiencies and probe light's resonant absorption. Simulation data for $\Delta k = 0$ (dashed) and Δk with approximations (dotted, small in the gain region and larger elsewhere) are also presented.

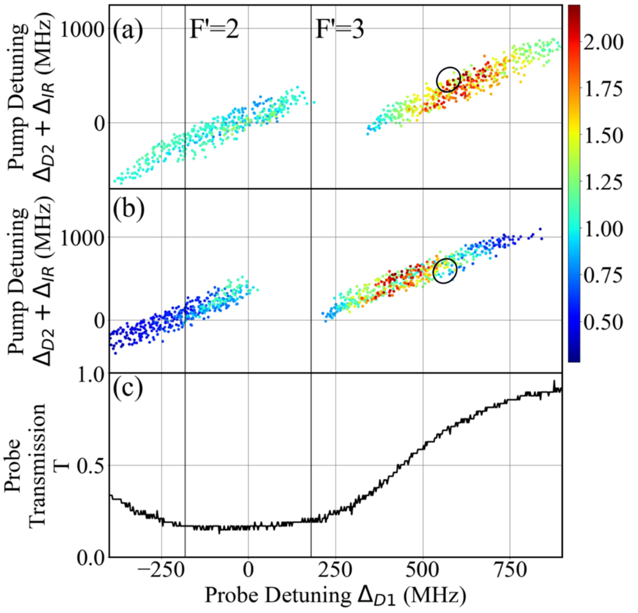

Fig. 3. FWM gain map: maximum measured values of probe gain (a) G_P and conjugate gain (b) G_C as a function of optimal probe detuning Δ_{D1} (horizontal axis) and total two-photon pump detuning $\Delta_{D1} + \Delta_{D2}$ (vertical axis). (c) Unamplified probe transmission (without pump fields). The region where maximum intensity squeezing is achieved is highlighted with a black circle. The same pump laser powers as in Fig. 2 are used: $P_{D2} = 260$ mW and $P_{IR} = 33$ mW.

this region. The reasonable agreement between the experimental data and the simulated results is illustrated in Fig. 2.

Figure 3 provides further insight into the FWM dependence on the frequencies of the pump lasers. Each data point represents the highest values of FWM gain for a given combination of the probe laser detuning Δ_P and the two-photon pump detuning $\Delta_{D2} + \Delta_{IR}$. To attain these gain values, we recorded the dependence of probe and conjugate gains on the probe laser frequency for specific two-photon detunings (an example spectrum is shown in Fig. 2), identified the highest FWM gain peaks, and recorded their amplitudes and frequency positions. We clearly observe two spectral regions of FWM amplification, separated by approximately 400 MHz in probe detuning (corresponding to the hyperfine structure of the $5P_{1/2}$ level). These regions are also shifted "vertically" due to the combined effects of the hyperfine structures of the $6S_{1/2}$ and $5P_{3/2}$ levels. In our experiments, we focus on the higher frequency region ($\Delta_P \approx 500$–800 MHz), which corresponds to higher FWM gain and lower resonant absorption. Figure 3 also illustrates the necessary compromise between FWM gain and resonant absorption of the probe field. For instance, the highest values of G_C occur closer to the D1 line transition of ^{85}Rb, while maximum G_P is shifted toward higher probe detunings. This can be explained by the probe field near the optical resonance [as shown in Fig. 3(c)], which directly affects the output power of the probe field. In contrast, the conjugate field experiences negligible atomic absorption, so its output power is primarily determined by the strength of the FWM process. To observe intensity squeezing, we need to equalize the FWM gains for both optical components, which can be maximally approached in the region of experimental parameters marked by circles in Figs. 3(a) and 3(b).

After identifying the optimal experimental configuration to maximize FWM efficiency, the next step involved measuring and analyzing the relative intensity noise of the probe and conjugate fields. To determine the presence of nonclassical correlations between these two fields, we electronically subtracted their photocurrents and analyzed the resulting noise power spectrum using a spectrum analyzer. We characterized the degree of quantum correlations using the squeezing parameter, S, where

$$S = 10\log_{10}\left[\frac{\mathrm{Var}(\hat{n}_P - \hat{n}_C)}{\langle\hat{n}_P\rangle + \langle\hat{n}_C\rangle}\right], \tag{3}$$

where $\hat{n}_P$ and $\hat{n}_C$ are the number operators describing the photon flux in each optical field, proportional to the photoelectron flux operators. According to this definition, the shot-noise limit—representing the relative noise power of two independent coherent fields—corresponds to $S = 0$. When the photon numbers in the two fields are correlated quantumly, the joint differential variance (Var) in the numerator becomes smaller than the total fluctuation in the denominator, resulting in negative values of S. A larger negative value of S indicates better intensity squeezing. In line with quantum optics, both the probe and conjugate fields exhibit super-Poissonian statistics, implying that each field is noisier than a coherent field with the same mean photon number.

Figure 4 presents representative measurements of the relative intensity noise for both the probe and conjugate optical fields, along with their respective individual noise levels. The shot-noise level (indicated by the horizontal black line) is computed based on the photodiodes' calibration using coherent state inputs. As anticipated, each of the probe and conjugate fields

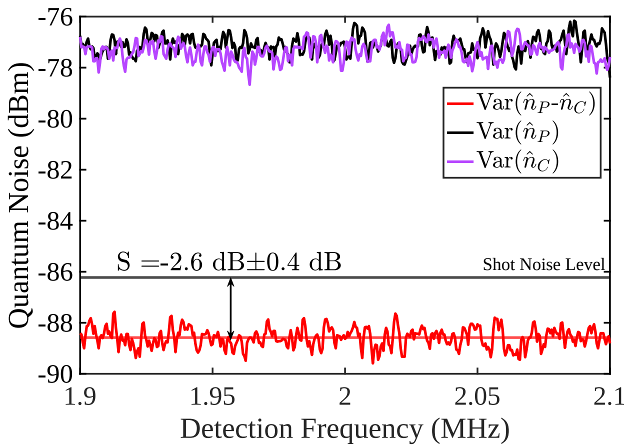

Fig. 4. The variance of the relative photocurrent noise spectrum (red), Var($\hat{n}_P - \hat{n}_C$), for the probe and conjugate fields, along with their individual intensity noise levels, Var($\hat{n}_{P/C}$) (black/purple). As reference, the black straight line marks the shot-noise level, Var($\hat{n}_P^{(coh)} - \hat{n}_C^{(coh)}$), measured for two coherent laser fields. The relevant detunings are $\Delta_{D1} \approx 800$ MHz, $\Delta_{D2} = -280$ MHz, and $\Delta_{IR} = 800$ MHz, with two pump laser powers of $P_{D2} = 350$ mW and $P_{IR} = 32$ mW, respectively.

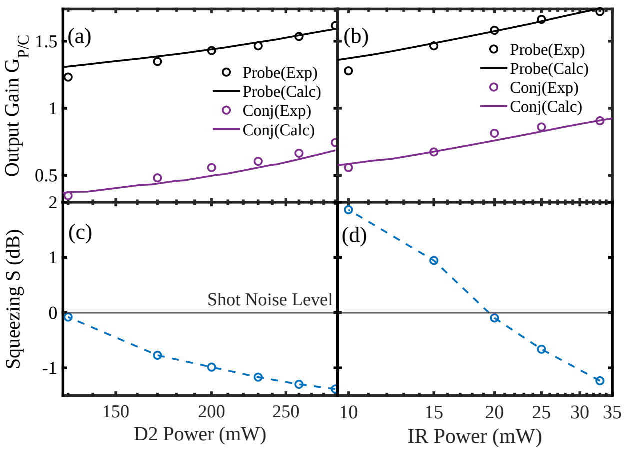

Fig. 5. Dependence of (a),(b) the FWM gain $G_{P/C}$ and (c),(d) relative intensity squeezing on the pump laser powers. Panels (a) and (c) show data for varying D2 pump power with fixed IR pump power at $P_{IR} = 35$ mW, while (b),(d) correspond to varying IR pump power with fixed D2 pump power at $P_{D2} = 290$ mW. The solid lines represent theoretical gain predictions from the numerical model, while the dashed lines in the squeezing data provide a visual guide. The small hollow circles denote the experimentally measured values.

displays an excess noise of +9 dB above the shot-noise level when measured independently. In contrast, the differential photocurrent noise is reduced by −2.6 dB below the shot-noise level, indicating the emergence of quantum correlations. This degree of squeezing was achieved with a probe field gain of $G_P = 2.08$ and an 85% transmission without the occurrence of FWM (measured with the IR pump laser blocked). The corresponding gain for the conjugate field was $G_C = 1.45$, with no observable resonant absorption.

To compare the measured squeezing values with the theoretically expected performance, it is imperative to account for optical losses during beam propagation. Neglecting the contributions of Langevin forces due to minor resonant absorption, we employ a distributed beam splitter model. In this approach, the interaction volume is divided into N slices, and the output quantum fields are calculated using the FWM gain and loss in each slice, as described in the Supplement 1. Under these conditions, Eq. (3) is modified as follows:

$$S = 10\log_{10}\left[\frac{(G_P - G_C)\langle \hat{n}_{P,z=0}\rangle + \sum_1^N \chi_{a,i}(\langle \hat{n}_{P,z=0}\rangle + 1)}{(G_P + G_C)\langle \hat{n}_{P,z=0}\rangle}\right], \qquad (4)$$

where $\chi_{a,i}$ contains the added vacuum fluctuation contributions due to losses for the ith slice of the atomic ensemble, as detailed in Section 3 of the Supplement 1. Equation (4) now offers a reasonable estimate of the expected squeezing level. For parameters similar to the experimental conditions in Fig. 4, the predicted two-mode squeezing level is approximately −3 dB. Typically, the model predictions are 1–2 dB below the experimentally measured values.

The primary source of additional noise is the phase noise of the probe laser, which is converted into intensity noise near the atomic resonance. When only the probe field is present in the cell, its intensity noise increases by 1 to 3 dB at this detuning, while it remains at the shot-noise level when the laser is far-detuned. This noise is carried through the amplification process, causing each individual beam to exhibit more noise than anticipated. Although this extra technical noise is partially canceled in the differential intensity measurements, the cancellation is incomplete due to the differing gain values for the two fields. Additional technical noise also arises from thermal fluctuations and laser polarization instabilities.

For our system to become practical for QIS applications, its performance must improve to achieve a level of squeezing (and eventually entanglement) suitable for real-world use. For instance, an entanglement threshold of around −9 dB is demanded for implementing hybrid photon conversion protocols [6]. To enhance squeezing, we need to acquire higher gain and reduce losses. However, adjusting laser detunings can only optimize one at the expense of the other. The most promising and straightforward approach is increasing the pump laser intensity. Figures 5(a)–5(d) show experimental results alongside numerical simulations of the FWM gains G_P and G_C, as well as the measured squeezing parameter S over a range of pump powers. The results clearly demonstrate that increasing laser power improves system performance.

To explore potential improvements in achievable FWM gain and squeezing levels at higher laser powers, we performed simulations over an extended pump power range (beyond what is currently attainable with the lasers available for this experiment). In these simulations, the laser detunings were fixed near the experimental values: $\Delta_{D1} \approx 400 - 800$ MHz, $\Delta_{D2} = -280$ MHz, and $\Delta_{IR} = 800$ MHz. The results are presented in Fig. 6. It is evident that increasing the IR pump power consistently leads to higher FWM gain for both the probe and conjugate fields, resulting in greater levels of squeezing. Initially, increasing the D2 pump power also boosts the gain, but it eventually reaches a peak at a value that depends on the available IR pump power. As the IR power increases, the maximum FWM gain shifts to a higher D2 power range, as shown in Figs. 6(a) and 6(b). The predicted squeezing values in Fig. 6(c), obtained using Eq. (4) and accounting for probe field optical losses calculated for each

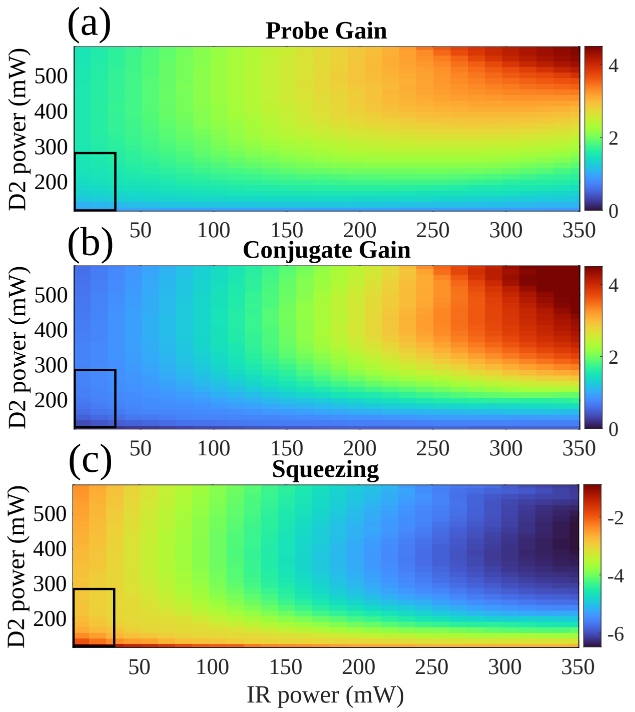

Fig. 6. Theoretically predicted FWM gain values for (a) the probe and (b) conjugate output fields are shown over a wider range of pump laser powers. The calculations assume detunings of $\Delta_{D2} \approx -280$ MHz, $\Delta_{IR} \approx 800$ MHz. To locate the maximum FWM gain peak, we adjust Δ_{D1} from approximately 400 to 800 MHz, accounting for the light shift caused by the vastly different pump powers. (c) Predicted differential intensity squeezing is shown, based on the calculated gain values and the residual resonant absorption of the probe field, using a beam splitter model. The black squares represent the range of pump powers used in the experiment.

configuration, indicate that with reasonable laser powers, up to 6.5 dB of two-mode intensity squeezing can be achieved.

In principle, further steps can be taken to improve the squeezing. The large wavelength difference between the optical fields in thermal atoms significantly limits the fraction of atoms participating in the FWM process, while all atoms contribute to resonant loss. Introducing velocity-selective pumping could preferentially prepare atoms in the desired velocity group, enhancing the FWM strength without imparting additional loss. Preliminary studies [29] have shown some improvement in FWM gain with use of a counter-propagating pumping field, though its effect on quantum properties has yet to be fully explored.

In conclusion, we have demonstrated an atom-based narrowband source of two-mode intensity correlations between optical fields at different wavelengths: a 795 nm probe field resonant with the ^{85}Rb atomic resonance and a 1324 nm conjugate field, falling within the telecom O-band. This was achieved using four-wave mixing in a double-ladder configuration, with two pump lasers of moderate power (up to 350 mW for the 780 nm laser and up to 35 mW for the 1367 nm laser). The maximum achieved gain G_P exceeded 2, with up to 85% residual resonant absorption for the probe field. Under optimized conditions, we observed up to −2.6 dB of relative photocurrent noise suppression below the shot-noise level, clearly demonstrating nonclassical correlations between the intensity fluctuations of the two optical fields. Our theoretical model predicts that up to 6 dB relative-intensity squeezing could be reachable with higher laser power and reduced residual noise.

Funding. U.S. Department of Energy (DE-SC0022069).

Acknowledgments. Z.N. and I.N. thank Nicolas Destefano and Eugeniy E. Mikhailov for their help with the experiment.

Disclosures. The authors declare no conflicts of interest.

Data availability. Data underlying the results presented in this paper are not publicly available at this time but may be obtained from the authors upon reasonable request.

Supplemental document. See Supplement 1 for supporting content.

REFERENCES AND NOTE

1. L.-M. Duan, M. D. Lukin, J. I. Cirac, *et al.*, "Long-distance quantum communication with atomic ensembles and linear optics," Nature **414**, 413–418 (2001).
2. K. Azuma, S. E. Economou, D. Elkouss, *et al.*, "Quantum repeaters: From quantum networks to the quantum internet," Rev. Mod. Phys. **95**, 045006 (2023).
3. H. J. Kimble, "The quantum internet," Nature **453**, 1023–1030 (2008).
4. S. Wehner, D. Elkouss, and R. Hanson, "Quantum internet: A vision for the road ahead," Science **362**, eaam9288 (2018).
5. S. Takeda, T. Mizuta, M. Fuwa, *et al.*, "Deterministic quantum teleportation of photonic quantum bits by a hybrid technique," Nature **500**, 315–318 (2013).
6. X.-W. Luo, C. Zhang, I. Novikova, *et al.*, "Wavelength conversion for single-photon polarization qubits through continuous-variable quantum teleportation," Phys. Rev. A **105**, 052444 (2022).
7. M. Allgaier, V. Ansari, L. Sansoni, *et al.*, "Highly efficient frequency conversion with bandwidth compression of quantum light," Nat. Commun. **8**, 14288 (2017).
8. X. Wang, X. Jiao, B. Wang, *et al.*, "Quantum frequency conversion and single-photon detection with lithium niobate nanophotonic chips," npj Quantum Inf **9**, 38 (2023).
9. R. Willis, F. Becerra, L. Orozco, *et al.*, "Four-wave mixing in the diamond configuration in an atomic vapor," Phys. Rev. A **79**, 033814 (2009).
10. R. T. Willis, *Photon pair production from a hot atomic ensemble in the diamond configuration* (University of Maryland, College Park, 2009).
11. A. N. Craddock, Y. Wang, F. Giraldo, *et al.*, "High-rate subgigahertz-linewidth bichromatic entanglement source for quantum networking," Phys. Rev. Appl. **21**, 034012 (2024).
12. F. Becerra, R. Willis, S. Rolston, *et al.*, "Nondegenerate four-wave mixing in rubidium vapor: The diamond configuration," Phys. Rev. A **78**, 013834 (2008).
13. A. Radnaev, Y. Dudin, R. Zhao, *et al.*, "A quantum memory with telecom-wavelength conversion," Nat. Phys. **6**, 894–899 (2010).
14. C.-Y. Hsu, Y.-S. Wang, J.-M. Chen, *et al.*, "Generation of sub-MHZ and spectrally-bright biphotons from hot atomic vapors with a phase mismatch-free scheme," Opt. Express **29**, 4632–4644 (2021).
15. S. L. Braunstein and P. van Loock, "Quantum information with continuous variables," Rev. Mod. Phys. **77**, 513–577 (2005).
16. C. Weedbrook, S. Pirandola, R. García-Patrón, *et al.*, "Gaussian quantum information," Rev. Mod. Phys. **84**, 621–669 (2012).
17. P. Wang, M. Chen, N. C. Menicucci, *et al.*, "Weaving quantum optical frequency combs into continuous-variable hypercubic cluster states," Phys. Rev. A **90**, 032325 (2014).
18. P. C. Humphreys, W. S. Kolthammer, J. Nunn, *et al.*, "Continuous-variable quantum computing in optical time-frequency modes using quantum memories," Phys. Rev. Lett. **113**, 130502 (2014).
19. N. Liu, J. Thompson, C. Weedbrook, *et al.*, "Power of one qumode for quantum computation," Phys. Rev. A **93**, 052304 (2016).
20. G. Adesso, S. Ragy, and A. R. Lee, "Continuous variable quantum information: Gaussian states and beyond," Open Syst. Inf. Dyn. **21**, 1440001 (2014).

21. N. Killoran, T. R. Bromley, J. M. Arrazola, *et al.*, "Continuous-variable quantum neural networks," Phys. Rev. Res. **1**, 033063 (2019).
22. U. Andersen, G. Leuchs, and C. Silberhorn, "Continuous-variable quantum information processing," Laser Photonics Rev. **4**, 337–354 (2010).
23. C. McCormick, A. M. Marino, V. Boyer, *et al.*, "Strong low-frequency quantum correlations from a four-wave-mixing amplifier," Phys. Rev. A **78**, 043816 (2008).
24. V. Boyer, A. M. Marino, R. C. Pooser, *et al.*, "Entangled images from four-wave mixing," Science **321**, 544–547 (2008).
25. Q. Glorieux, R. Dubessy, S. Guibal, *et al.*, "Double-λ microscopic model for entangled light generation by four-wave mixing," Phys. Rev. A **82**, 033819 (2010).
26. H.-R. Noh and H. S. Moon, "Four-wave mixing in a ladder configuration of warm^{87} Rb atoms: a theoretical study," Opt. Express **29**, 6495–6508 (2021).
27. G. Morigi, S. Franke-Arnold, and G.-L. Oppo, "Phase-dependent interaction in a four-level atomic configuration," Phys. Rev. A **66**, 053409 (2002).
28. M. Jasperse, *Relative Intensity Squeezing by Four-Wave Mixing in Rubidium* (2010).
29. Z. Niu, J. Wen, C. Zhang, *et al.*, "Toward bi-chromatic intensity squeezing using double-ladder four-wave mixing in 85rb," in *Quantum Sensing, Imaging, and Precision Metrology II*, Vol. 12912 (SPIE, 2024), pp. 6–17.
30. Due to the limited accuracy of the wavemeter used for pump frequency calibration, the exact pump detuning values are determined by comparing the numerical model with the measured data.

195.252.220.43 {ts '2025-01-30 23:35:58'}